An integrated inductor for parallel interleaved VSCs connected in a whiffletree configuration

Gohil, Ghanshyamsinh; Bede, Lorand; Teodorescu, Remus; Kerekes, Tamas; Blaabjerg, Frede

Published in:
Proceedings of the 2015 IEEE Energy Conversion Congress and Exposition (ECCE)

DOI (link to publication from Publisher):
10.1109/ECCE.2015.7310495

Publication date:
2015

Document Version
Publisher's PDF, also known as Version of record

An Integrated Inductor for Parallel Interleaved VSCs Connected in a Whiffletree Configuration

Ghanshyamsinh Gohil, Lorand Bede, Remus Teodorescu, Tamas Kerekes, Frede Blaabjerg
Department of Energy Technology, Aalborg University, Denmark
gvg@et.aau.dk

***Abstract*—The quality of voltage waveform of the parallel connected inverters can be improved by interleaving the carrier signals. However, an additional coupled inductors (CIs) are required to suppress the circulating current between the interleaved VSCs and often connected in a whiffletree configuration. The integration of the line filter inductor and the coupled inductors in a single magnetic component for such systems is proposed. The fundamental frequency component of the flux is confined to the limbs around which the coils are placed, whereas other parts only experiences high frequency flux excitation. As a result, the inductor can be made smaller. The inductor is analyzed and performance is verified by simulation and experimental studies.**

I. Introduction

In many high power applications, the two-level VSCs are normally connected in parallel to meet the high current requirement and often share the common dc-link, as shown in Fig. 1. The high power VSCs suffer from excessive losses if the switching frequency is increased beyond a few kHz. Due to the limited switching frequency, large passive filter components are generally employed to comply with the stringent power quality requirements. The large passive filter components lead to the increased cost, size and losses. Therefore the efforts should be made to reduce the size of these components. For a given switching frequency, the filtering requirement can be reduced by employing a multilevel VSC.

For the parallel connected two-level VSCs, multi-level voltage waveforms can be achieved by interleaving the carrier signals. As a result of the interleaved carriers, some of the harmonic frequency components present in the switched output voltage of the parallel interleaved legs are phase shifted with respect to each other [1]–[7]. For the parallel connected VSCs, the output voltage of a particular phase is the average of the switched output voltage of all parallel VSC legs of that phase. As a result of the averaging, the contribution of the phase shifted harmonic frequency components of the individual switched output voltages is fully or partially canceled in the resultant voltage [8]. This leads to the reduction in the value of the filter components [9].

When connected to a common dc-link, the circulating current flows between the parallel VSCs due to the hardware and control asymmetries, as shown in Fig. 1. The interleaving of the carrier signals further aggravates the already existing problem of the circulating current. This unwanted circulating current increases the losses in both the semiconductor devices and in the passive components and it should be suppressed. An additional inductive filter is often required for this purpose. A

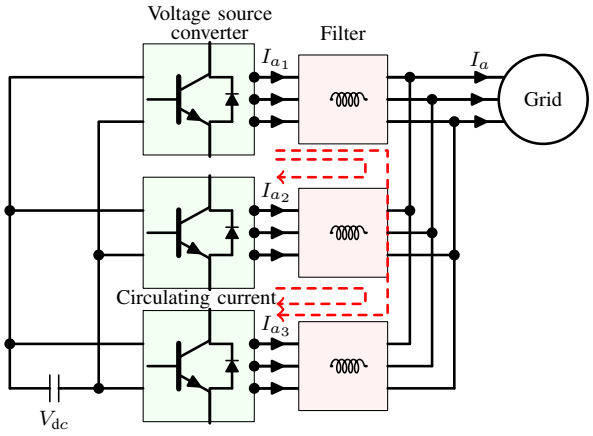

Fig. 1. Parallel voltage source converters with a common dc-link and output filters.

Coupled Inductor (CI) can effectively suppress the circulating current by providing magnetic coupling between the parallel interleaved legs of the corresponding phases [1], [10]–[15]. For the multiple parallel VSCs, the CIs are often connected in a whiffletree configurations, as proposed in [1]. Such arrangement requires two distinct inductive component:

1) Line filter inductor (L_f) for improving the injected line current quality.
2) CIs for suppressing the circulating current.

The volume of the inductive component can be reduced by integrating both of these functionalities into a single magnetic component. This paper proposes the magnetic integration of the line filter inductor L_f and the circulating current filters (which mainly experiences the switching frequency flux excitation) for a four parallel interleaved VSCs. The VSCs are divided into two converter groups and the VSCs carrier signals of the VSCs within each group are shifted by $180°$. The issue of the circulating current and the overview of the existing filtering solutions are briefly discussed in Section II. The proposed integrated inductor is analyzed in Section III. The design of the coupled inductor that is used for circulating current suppression between the two converter groups is discussed in Section IV. The volume reduction achieved by the proposed solution is demonstrated in Section V, by comparing it with the state-of-the-art solution. The functionality of the integrated inductor is verified by performing simulation and experimental

978-1-4673-7151-3/15/$31.00 ©2015 IEEE

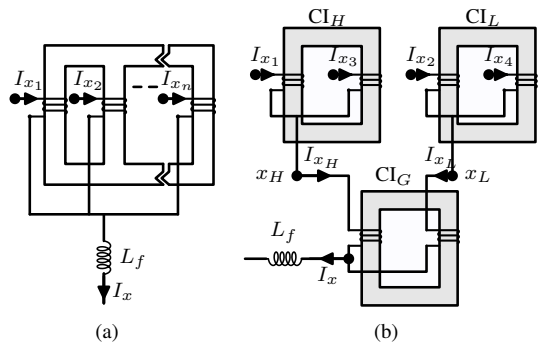

Fig. 2. Various arrangements of the filters for the parallel interleaved VSCs. (a) CI with $N-$limb core structure, (b) Whiffletree configuration using the two limb CIs. The subscript x represents phases $x = \{a, b, c\}$.

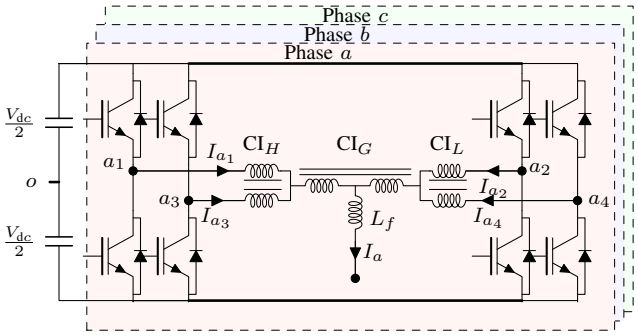

Fig. 3. Whiffletree configuration for parallel interleaved voltage source converters.

studies and the results are presented in Section VI.

II. Circulating Current in a Parallel Interleaved VSCs

The switched output voltages of the parallel legs are phase shifted with respect to each other due to the interleaved carriers. When parallel VSCs are connected to the common dc-link, this instantaneous potential difference appears across the closed path and gives rise to the circulating current. The circulating current can be suppressed by introducing sufficiently high inductance in that closed current path. The CI provides magnetic coupling between the interleaved legs of a particular phase and offers high inductance to the circulating current, while its effect on the line current is minimal (considering negligible flux leakage).

The various possible arrangements of the CI is shown in Fig. 2. Fig. 2(a) shows the magnetic structure of the CI using n parallel limbs for n parallel VSCs. This magnetic structure is asymmetrical, when more than two limbs are used. The symmetry can be achieved by using a whiffletree configuration. The parallel interleaved VSCs with whiffletree configuration is shown in Fig. 3. Two limb CI is used as a building block and the filter arrangement is shown in Fig. 2(b). Two interleaved legs of a respective phase are magnetically coupled using the CI (CI_H and CI_L in Fig. 3) and for the four VSCs, two such pairs are also magnetically coupled using the third CI

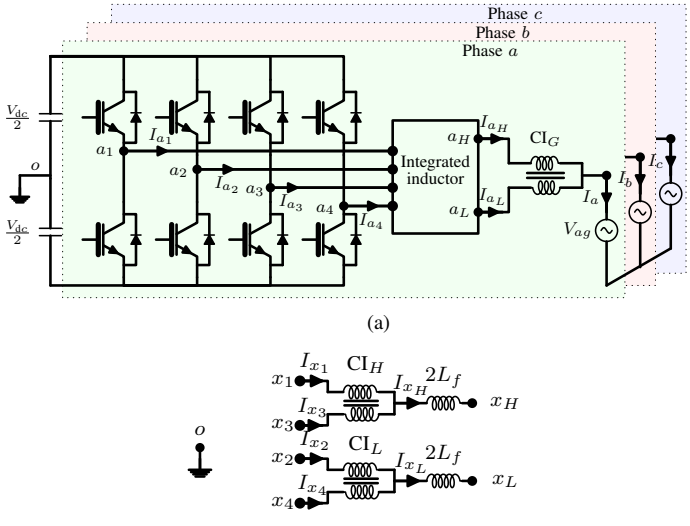

Fig. 4. Four parallel interleaved VSCs with the proposed integrated inductor. (a) System schematic, (b) Equivalent electrical model of the integrated inductor. The subscript x represents phases $x = \{a, b, c\}$

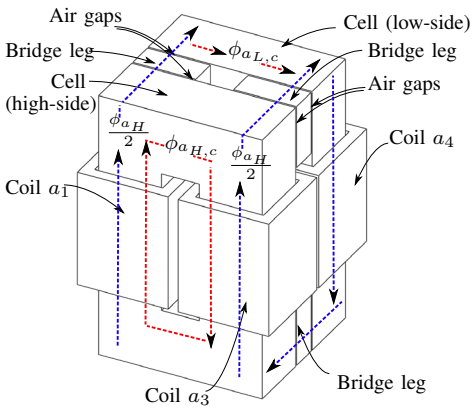

Fig. 5. Magnetic structure of the proposed integrated inductor.

(CI_G). The proposed integrated inductor, which combines the functionality of the line filter inductor L_f and the CI_H and the CI_L (refer Fig. 2(b)), is presented in the following Section.

III. Integrated Inductor

The system comprises of four parallel VSCs with the proposed integrated inductor as shown in Fig. 4(a). All four VSCs share a common dc-link and the carrier signals are symmetrically interleaved, i.e. the carrier signals are phase shifted from each by $90°$. The carrier signals of the VSC1 and VSC3 are phase shifted by $180°$ from each other and these two VSCs form the High-Side Converter Group (HSCG). Similarly, VSC2 and VSC4 forms the Low-Side Converter Group (LSCG), with carrier signals phase shifted from each other by $180°$.

The proposed integrated inductor is shown in Fig. 5. The magnetic structure comprises of two cells. The cell is a two limb CI structure and each limb carries a coil with N number

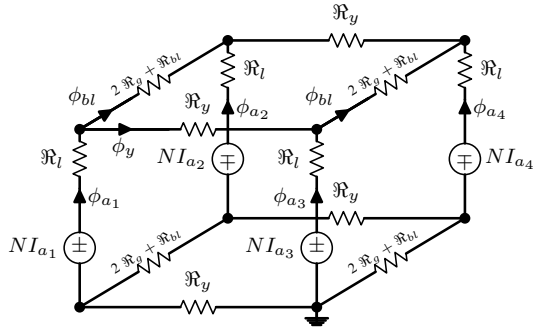

Fig. 6. Simplified reluctance model of the proposed integrated inductor.

of turns. Both of these coils in the cell are wound in the same direction. The limbs are magnetically coupled to each other using the top and the bottom yokes. Intentional air gap is avoided in the cell structure.

Out of the two cells, one of the cells magnetically couples the interleaved legs of the respective phases of the HSCG, whereas the other cell belongs to the LSCG. The input terminals of the coils of the high-side cell are connected to the output of VSC1 (a_1) and VSC3 (a_3) and the output terminals of these coils are connected together to form the common output a_H. Similarly, the output of VSC2 (a_2) and VSC4 (a_4) are connected to the input terminal of the coils of the low-side cell. Whereas, the other end of the coils are connected together to form the common output terminal a_L. The winding direction of the coils of the high-side cell is opposite to that of the coils of the low-side cell. The high-side and the low-side cells are magnetically coupled to each other using the bridge legs, as shown in Fig. 5. The necessary air gaps have been inserted between the cells and the bridge legs. The output terminals of the HSCG and the LSCG are connected to another CI (CI_G), as shown in Fig. 4(a).

A. Magnetic Circuit Analysis

The integrated inductor is analyzed in this sub section. Due to the phase symmetry, the analysis is done for one of the phases. The phases a, b, and c are represented by subscript x. For the system shown in Fig. 4(a), the voltage across the coil x_1 is given as

$$\begin{aligned} V_{x_1x_H} =& L_{x_1x_1}\frac{dI_{x_1}}{dt} + L_{x_1x_2}\frac{dI_{x_2}}{dt} \\ &+ L_{x_1x_3}\frac{dI_{x_3}}{dt} + L_{x_1x_4}\frac{dI_{x_4}}{dt} \end{aligned} \tag{1}$$

where $L_{x_jx_k}$ is the inductance between the jth and the kth coil of the integrated inductor of phase x and I_{x_n} is the current flowing through the nth coil of phase x. The simplified reluctance model of the integrated inductor is shown in Fig. 6. The reluctance of each of the limbs and the yoke of the cell are $\Re_l$ and $\Re_y$, respectively. The reluctance of the bridge leg is $\Re_{bl}$, whereas the reluctance of each of the air gaps is denoted by $\Re_g$. The magneto-motive force of the coil is represented as NI_{x_n}.

The flux in each limb is given as

$$\overrightarrow{\phi} = \frac{1}{\Re_l}\boldsymbol{R}\left(\frac{1}{\Re_l}\boldsymbol{A} + \boldsymbol{R}\right)^{-1}\overrightarrow{\boldsymbol{M}} \tag{2}$$

where $\boldsymbol{A}$ is the unit matrix,

$$\overrightarrow{\phi} = \begin{bmatrix}\phi_{x_1} & \phi_{x_2} & \phi_{x_3} & \phi_{x_4}\end{bmatrix}^T \tag{3}$$

$$\overrightarrow{\boldsymbol{M}} = \begin{bmatrix}NI_{x_1} & -NI_{x_2} & NI_{x_3} & -NI_{x_4}\end{bmatrix}^T \tag{4}$$

$$\overrightarrow{\boldsymbol{R}} = \begin{bmatrix} \frac{1}{\Re_{eq}} & -\frac{1}{\Re_2} & -\frac{1}{\Re_1} & 0 \\ -\frac{1}{\Re_2} & \frac{1}{\Re_{eq}} & 0 & -\frac{1}{\Re_1} \\ -\frac{1}{\Re_1} & 0 & \frac{1}{\Re_{eq}} & -\frac{1}{\Re_2} \\ 0 & -\frac{1}{\Re_1} & -\frac{1}{\Re_2} & \frac{1}{\Re_{eq}} \end{bmatrix} \tag{5}$$

where $\Re_1 = 2\Re_y$, $\Re_2 = 4\Re_g + 2\Re_{bl}$, and $\frac{1}{\Re_{eq}} = \frac{1}{\Re_1} + \frac{1}{\Re_2}$. By assuming $\Re_g$ is very high compared to the other reluctances in the network and solving the reluctance network, the inductances specified in (1), can be obtained as

$$\begin{aligned} L_{x_1x_2} = L_{x_1x_4} = L_{M_1} \approx \frac{N^2}{8\Re_g} \\ L_{x_1x_3} = L_{M_2} \approx -\frac{N^2}{2\Re_l + \Re_1} \end{aligned} \tag{6}$$

$$L_{x_1x_1} = L_{x_2x_2} = L_{x_3x_3} = L_{x_4x_4} = L_S \approx 2L_{M_1} - L_{M_2} \tag{7}$$

Substituting these inductances in (1) gives

$$\begin{aligned} V_{x_1x_H} &= V_{x_1o} - V_{x_Ho} \\ &= L_S\frac{dI_{x_1}}{dt} + L_{M_1}\frac{d(I_{x_2}+I_{x_4})}{dt} + L_{M_2}\frac{dI_{x_3}}{dt} \end{aligned} \tag{8}$$

Similarly, the voltages across other coils can be given as

$$\begin{aligned} V_{x_2x_L} &= V_{x_2o} - V_{x_Lo} \\ &= L_{M_1}\frac{d(I_{x_1}+I_{x_3})}{dt} + L_S\frac{dI_{x_2}}{dt} + L_{M_2}\frac{dI_{x_4}}{dt} \end{aligned} \tag{9}$$

$$\begin{aligned} V_{x_3x_H} &= V_{x_3o} - V_{x_Ho} \\ &= L_{M_2}\frac{dI_{x_1}}{dt} + L_S\frac{dI_{x_3}}{dt} + L_{M_1}\frac{d(I_{x_2}+I_{x_4})}{dt} \end{aligned} \tag{10}$$

$$\begin{aligned} V_{x_4x_L} &= V_{x_4o} - V_{x_Lo} \\ &= L_{M_2}\frac{dI_{x_2}}{dt} + L_{M_1}\frac{d(I_{x_1}+I_{x_3})}{dt} + L_S\frac{dI_{x_4}}{dt} \end{aligned} \tag{11}$$

The output current of each of the VSCs has a common current component and the circulating current component. The output currents of HSCG and LSCG are given as

$$I_{x_H} = I_{x_1} + I_{x_3}\ ,\ I_{x_L} = I_{x_2} + I_{x_4} \tag{12}$$

Assuming equal current sharing between the VSCs, the common component of each of the VSCs is taken to be the same. Therefore, the output current of the individual VSCs are given as

$$\begin{aligned} I_{x_1} = \frac{I_{x_H}}{2} + I_{x_{H,c}}\ ,\ I_{x_3} = \frac{I_{x_H}}{2} - I_{x_{H,c}} \\ I_{x_2} = \frac{I_{x_L}}{2} + I_{x_{L,c}}\ ,\ I_{x_4} = \frac{I_{x_L}}{2} - I_{x_{L,c}} \end{aligned} \tag{13}$$

where $I_{x_{H,c}}$ and $I_{x_{L,c}}$ are the circulating current between the VSCs of the HSCG and the LSCG, respectively. The resultant

line current and the circulating current between the high-side and the low-side converter groups are given as

$$I_x = I_{x_L} + I_{x_H}\ ,\ I_{x,c} = \frac{I_{x_H} - I_{x_L}}{2} \tag{14}$$

where $I_{x,c}$ is the circulating current between the HSCG and the LSCG and it is suppressed using the CI_G.

B. Inductance offered by the integrated inductor

Averaging (8) and (10) gives

$$\begin{aligned}\left(\frac{V_{x_1o} + V_{x_3o}}{2}\right) - V_{x_Ho} &= L_{M_1}\left(\frac{dI_{x_2}}{dt} + \frac{dI_{x_4}}{dt}\right) \\ &+ \left(\frac{L_S + L_{M_2}}{2}\right)\left(\frac{dI_{x_1}}{dt} + \frac{dI_{x_3}}{dt}\right)\end{aligned} \tag{15}$$

similarly, averaging (9) and (11) gives

$$\begin{aligned}\left(\frac{V_{x_2o} + V_{x_4o}}{2}\right) - V_{x_Lo} &= L_{M_1}\left(\frac{dI_{x_1}}{dt} + \frac{dI_{x_3}}{dt}\right) \\ &+ \left(\frac{L_S + L_{M_2}}{2}\right)\left(\frac{dI_{x_2}}{dt} + \frac{dI_{x_4}}{dt}\right)\end{aligned} \tag{16}$$

and using (15) and (16), the voltage drop across the line filter inductor is given as

$$\begin{aligned}V_{x_{avg}o} - V_{xo} &= \left(\frac{L_S + 2L_{M_1} + L_{M_2}}{4}\right)\frac{dI_{x_H}}{dt} \\ &+ \left(\frac{L_S + 2L_{M_1} + L_{M_2}}{4}\right)\frac{dI_{x_L}}{dt} \\ &= L_{M_1}\frac{dI_x}{dt}\end{aligned} \tag{17}$$

where

$$V_{x_{avg}o} = \frac{1}{4}\sum_{k=1}^{4} V_{x_ko} \text{ and } V_{xo} = \frac{V_{x_Ho} + V_{x_Lo}}{2} \tag{18}$$

using (17), the inductance offered to the line current is given as

$$L_f = L_{M_1} = \frac{\mu_0 N^2 A_g^{'}}{8 l_g} \tag{19}$$

where μ_0 is the permeability of the free space, l_g is the length of the air gap, and $A_g^{'}$ is the effective cross-section area of the air gap. The switched output voltage difference of VSC1 and VSC3 ($V_{x_1o} - V_{x_3o}$) drives the $I_{a_H,c}$. Similarly, the behavior of the $I_{a_L,c}$ depends on the difference of the switched output voltages of VSC2 and VSC4 ($V_{x_2o} - V_{x_4o}$). Using (8), (9), (10), and (11), the inductance offered to the circulating currents is given as

$$\begin{bmatrix} V_{x_1o} - V_{x_30} \\ V_{x_2o} - V_{x_40} \end{bmatrix} = \mathbf{L}\frac{d}{dt}\begin{bmatrix} I_{x_{H,c}} \\ I_{x_{L,c}} \end{bmatrix} \tag{20}$$

where the inductance matrix $\mathbf{L}$ is given as

$$\mathbf{L} = \begin{bmatrix} 4(L_{M_1} - L_{M_2}) & 0 \\ 0 & 4(L_{M_1} - L_{M_2}) \end{bmatrix} \tag{21}$$

C. Flux Density Analysis

The integrated inductor combines the functionalities of two CIs (CI_H and CI_L) and the line filter inductor L_f. Therefore, the flux in the magnetic core has distinct components corresponding to these inductances and it is analyzed in this sub section.

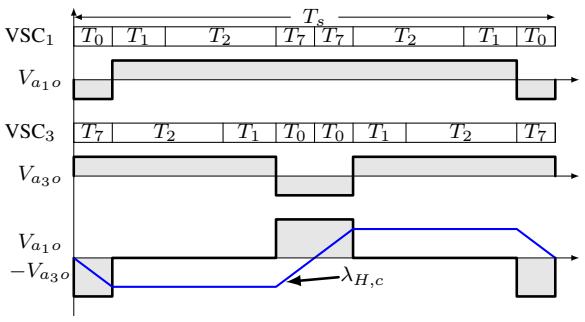

Fig. 7. Pole voltages of phase a of VSC1 and VSC3 and their difference for the 60° clamped discontinuous PWM (DPWM1) [18]. The modulation index $M = 1$ and voltage space vector angle $\psi = 45°$. Time T_o, T_1, T_2, and T_7 are the dwell times of the corresponding voltage vectors.

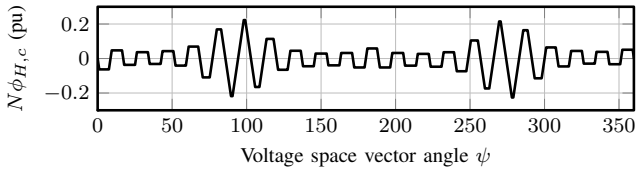

Fig. 8. Circulating flux component $\lambda_{H,c}$ over a complete fundamental period. The flux linkage is normalized to $V_{\text{dc}}T_s$.

1) Circulating Flux Component: From (20), the value of the circulating current flowing through the coil x_1 is obtained as

$$I_{x_{H,c}} = -\frac{1}{L_{M_2}}\int (V_{x_1o} - V_{x_3o})\, dt \tag{22}$$

and the circulating flux linkage can be obtained as [16], [17]

$$\lambda_{x_{H,c}} = N\phi_{x_{H,c}} = \frac{1}{2}\int (V_{x_1o} - V_{x_3o})\, dt \tag{23}$$

where $\phi_{x_{H,c}}$ is the circulating flux component in the high-side cell of the integrated inductor. The carrier signals of the VSC1 and VSC3 are interleaved by 180° and the corresponding voltages for a particular switching cycle is shown in Fig. 7. The VSCs are modulated using the space vector modulation [18]. Due to the change in the dwell time of the voltage vectors in each sampling interval, the peak value of the $\lambda_{x_{H,c}}$ also obtains different value in each of the sampling intervals. The $\lambda_{x_{H,c}}$ achieves the maximum value for the voltage space vector angle $\psi = 90°$ (and $\psi = 270°$), as shown in Fig. 8 and it is obtained as

$$\lambda_{x_{H,c_{max}}} = N\phi_{x_{H,c_{max}}} = \frac{V_{\text{dc}}}{8 f_s} \tag{24}$$

where V_{dc} is the dc-link voltage, f_s is the switching frequency, and $\phi_{H,c_{max}}$ is the maximum value of the circulating flux component.

For the LSCG, the carrier signals of the VSC2 and the VSC4 are also interleaved by 180° and the same analysis can be applied. The maximum value of the circulating flux component is also $N\phi_{x_{L,c_{max}}} = V_{\text{dc}}/8f_s$.

From the reluctance model, it is evident that the flux in the

yokes of the cell is equal to the resultant component of the circulating flux component $\phi_y = \phi_{x_{H,c}} = \phi_{x_{L,c}}$. Therefore, the maximum value of the flux density in the yokes is

$$B_{y_{max}} = \frac{V_{\text{dc}}}{8NA_{c_y}f_s} \tag{25}$$

2) Common Flux Component: The common current component of each of the VSCs can be decomposed into:

1) Fundamental frequency component.
2) Major harmonic components at the $4kf_s$, where $k = 1, 2, \ldots \infty$.

As the common flux component is proportional to the common current component, the common flux component is also composed of a fundamental frequency component and a ripple component. The fundamental component of the common flux component due to this current is

$$\phi_r(t) = \frac{\mu_0 N A_g^{'}}{8l_g} I_{x_{max}} \cos(\psi + \theta) \tag{26}$$

Normally the line filter inductance value is selected to limit the peak-to-peak value of the ripple component of the line current to the desired value. Let the ratio of the peak-to-peak value of the ripple component of the line current to the amplitude of the fundamental component of the line current be ε. For the space vector modulation, the ripple component attains its maximum value at the space vector angle of $\psi = 0°$. For unity power factor applications, the fundamental component is also maximum for the $\psi = 0°$. Therefore, the common flux component also attains its maximum value at the space vector angle of $\psi = 0°$ and it is given as

$$\phi_{r_{max}} = (1 + \frac{\varepsilon}{2}) \frac{\mu_0 N A_g^{'}}{8l_g} I_{x_{max}} \tag{27}$$

where $I_{x_{max}}$ is the amplitude of the rated current. The common component of the flux ϕ_r completes its path through the bridge legs, air gaps and legs of the cells. Therefore, the maximum value of the flux density in the bridge is given as

$$B_{bl_{max}} = (1 + \frac{\varepsilon}{2}) \frac{\mu_0 N A_g^{'}}{8l_g A_{c_{bl}}} I_{x_{max}} \tag{28}$$

3) Flux in the limbs of the cells: The flux that flows through the limbs of the cells, around which the coils are placed, is

$$\phi_l(t) = \phi_r(t) + \phi_{x_{H,c}}(t) \tag{29}$$

for the unity power factor applications ($\theta = 0$), the common component of the flux is maximum for $\psi = 0°$, whereas the circulating flux component $\phi_{x_{H,c}}$ is minimum at this voltage space vector angle. Similarly, the $\phi_{x_{H,c}}$ is maximum at $\psi = 90°$ and the common flux component is zero. Therefore, for the unity power factor applications

$$\phi_{l_{max}} = \max(\phi_{x_{H,c_{max}}}, \phi_{r_{max}} + \phi_{x_{H,c_{|\psi=0°}}}) \tag{30}$$

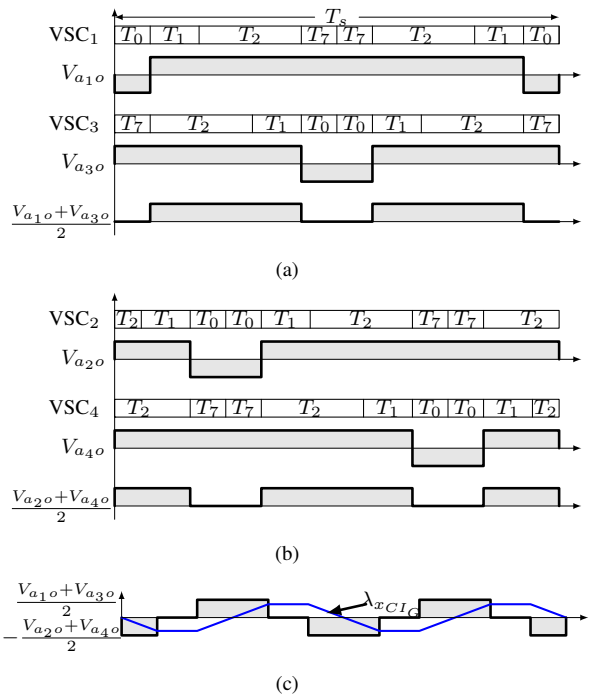

Fig. 9. Voltage waveforms for four parallel interleaved VSCs for $M = 1$ and $\psi = 45°$. (a) Pole voltages of the individual VSCs and their average voltage of the high side converter group, (b) Pole voltages of the individual VSCs and their average voltage of the low side converter group, (c) The difference of the average voltages of the high side converter group and the low side converter group and their associated flux linkage.

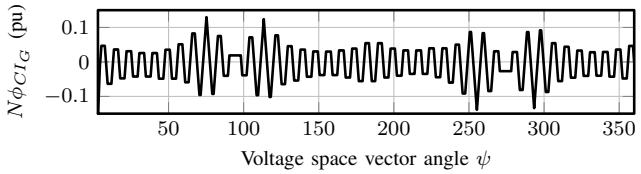

Fig. 10. Flux linkage of the CI_G ($\lambda_{x_{CI_G}}$) over a complete fundamental period. The flux linkage is normalized to $V_{\text{dc}}T_s$.

IV. Circulating Current Suppression Between the Two Converter Groups

The resultant output voltages of both the HSCG and LSCG are also phase-shifted with respect to each other and the circulating current flows between them due to these phase-shifted voltages. Additional CI (CI_G) is used to suppress this current.

The flux linkage in the CI_G is given as

$$N\phi_{x_{\text{CI}_G}} = \frac{1}{2} \int \left((\frac{V_{x_1o} + V_{x_3o}}{2}) - (\frac{V_{x_2o} + V_{x_4o}}{2}) \right) dt \tag{31}$$

The pole voltages of the individual VSCs and their average voltage for both the HSCG and the LSCG are shown in Fig. 9(a) and 9(b), respectively. The difference in the average voltages of both the converter groups and flux linkage of the CI_G is shown in Fig. 9(c). The flux linkage behavior over a fundamental period is also shown in Fig. 10. As it is evident,

TABLE I
SYSTEM PARAMETERS FOR SIMULATION AND EXPERIMENTAL STUDIES

Parameters	Values
Total power S	11 kVA
No. of VSCs	4
Interleaving angle	90°
DC-link voltage V_{dc}	650 V
Switching frequency f_s	1250 Hz
PWM scheme	SVM
Peak to peak value of the ripple current ε	25%
Line filter inductance L_f	2.3 mH (0.05 pu)

TABLE II
DESIGN PARAMETERS OF THE INTEGRATED INDUCTOR

Parameters	Values
Cross-section area of the limbs A_{c_l}	6.9×10^{-4} m^2
Cross-section area of the yokes A_{c_y}	6.9×10^{-4} m^2
Cross-section area of the bridge leg $A_{c_{bl}}$	4.8×10^{-4} m^2
Cross-section area of the air gap $A_g^{'}$	7.4×10^{-4} m^2
Length of the air gap l_g	9.6×10^{-4} m
Number of turns	N = 140
Cross section area of the conductor A_{cu}	1.31×10^{-6} m^2 (AWG 16)

the frequency of the flux reversal in the CI is $2 \times f_s$ and subjected to the half of the dc-link voltage. The maximum value of the flux density in the CI is given as

$$B_{CI_{G,max}} = \frac{V_{\text{dc}}}{32 N_{CI_G} A_{c_{CI_G}} f_s} \tag{32}$$

where N_{CI_G} and $A_{c_{CI_G}}$ are the number of turns in the coils and the cross section area of the CI, respectively.

V. DESIGN AND PERFORMANCE COMPARISON

The design details of the proposed inductor is discussed in this section. The size reduction achieved by a magnetic integration is demonstrated by comparing the volume of the proposed solution with the volume of the state-of-the-art solution.

A. Design

The integrated inductor and the CI$_G$ is designed using the design equations derived in section III and section IV for the converter system with four parallel VSCs. The system parameters are given in Table I. The integrated inductor and the CIG are designed to restrict the maximum value of the flux density to 0.7 T. Amorphous alloy 2605SA1 is used for the cells of integrated inductor and for the CI_G core, whereas laminated steel with a lamination thickness of 0.35 mm is used for the bridge legs. The parameters of the designed integrated inductor and the CI$_G$ are given in Table II and Table III, respectively.

B. Volumetric comparison

The volume of the different active materials of the magnetic components of the proposed filter arrangement is compared with the volume of the state-of-the-art solution, shown in Fig. 2(b). The line filter inductor in Fig. 2(b) is assumed made from the 0.35 mm laminated silicon steel. The amorphous alloys

TABLE III
DESIGN PARAMETERS OF THE COUPLED INDUCTOR CI$_G$

Parameters	Values
Cross-section area of the core $A_{c_{CI}}$	4.6×10^{-4} m^2
Number of turns N_{CI}	53
Cross section area of the conductor A_{cu}	2.62×10^{-6} m^2 (AWG 13)

TABLE IV
VOLUME COMPARISON OF THE ACTIVE MATERIALS OF THE MAGNETIC COMPONENTS IN THE PROPOSED SOLUTION WITH THE STATE-OF-THE-ART SOLUTION SHOWN IN FIG. 2(B)

Material	State-of-the-art	Proposed	% reduction
Amorphous alloy 2605SA1	1.477 Ltr.	1.221 Ltr.	17.3%
Laminated steel	0.281 Ltr.	0.143 Ltr.	49%
Copper	0.385 Ltr.	0.337 Ltr.	12.4 %

2605SA1 is considered as a magnetic material for the CIs (CI$_H$, CI$_L$, and CI$_G$ in Fig. 2(b)). The volume of the different materials in both the solutions are given in Table IV. The design of the CI$_G$ that is used to suppress the current between the HSCG and the LSCG is taken to be the same in both cases. In the state-of-art solution, the windings of the line filter inductor carries full line current and it is completely eliminated in the proposed solution. Therefore, the designer may choose to increase the number of turns in the coils of the integrated inductor to reduce the size of the amorphous alloy. In this comparison, the number of turns in the integrated inductor is taken to be 10% higher than the number of turns in the CI$_H$ and CI$_L$ in the state-of-the-art solution, as shown in Fig. 2(b). This results in the 17.3% saving in the amorphous alloy and 12.4% reduction in copper. Furthermore, the volume of the laminated steel is reduced by 49% in the proposed solution.

VI. SIMULATION AND THE EXPERIMENTAL RESULTS

The simulation and the experimental results for the four parallel interleaved VSCs are presented in this section. The system parameters are specified in Table I.

A. Simulation Results

The time domain simulation has been carried out using PLECS and the simulated flux density waveforms in the various parts of the magnetic structure of the integrated inductor and the CI$_G$ are shown in Fig. 11 and Fig. 12, respectively. Fig. 11(a), shows the flux density waveform in the limb of the cell, which is a vector addition of the common flux component and the circulating flux component. The circulating flux is confined to the cell and therefore the flux in the yoke has a switching frequency component as a major harmonic component, which is shown in Fig. 11(b). The common flux component flows out of the cell and completes its path through the air gaps and the bridge leg, as shown in Fig. 11(c). Due to the magnetic integration, the common flux component of the cell of the HSCG completes its path through the limbs of the cell of the LSCG and vice-versa. As a result, a dedicated return path is avoided. This brings in a substantial reduction of the volume of the integrated inductor.

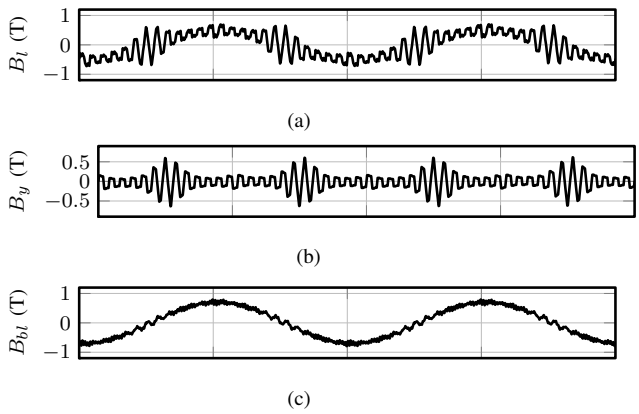

Fig. 11. Simulation results at rated operating conditions. (a) Flux density in the limb of the cell of the integrated inductor, (b) Flux density in yoke of the cell, (c) Flux density in the bridge leg.

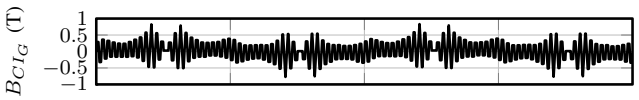

Fig. 12. Simulation results. (a) Flux density waveform in the coupled inductor that is used to suppress the circulating current between the high side and the low side converter group.

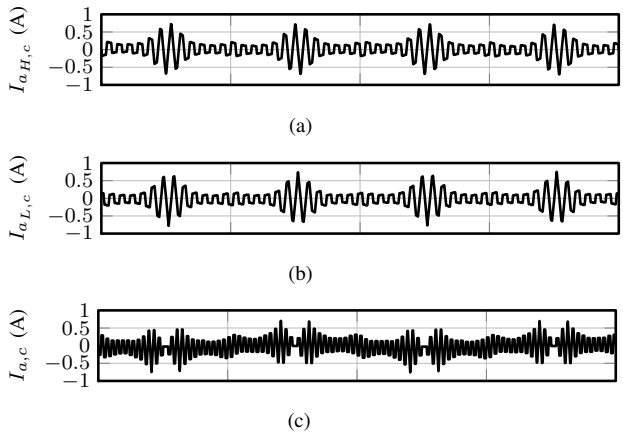

Fig. 13. Simulated current waveforms at rated operating conditions. (a) Circulating current between the VSCs of the high side converter group $I_{a_{H,c}}$, (b) Circulating current between the VSCs of the low side converter group $I_{a_{L,c}}$, (c) Circulating current between the high side converter group and the low side converter group $I_{a,c}$.

The circulating current between the HSCG and the LSCG is suppressed using the CI_G. The CI_G is subjected to half of the dc-link voltage and the flux has a major harmonic component at the 2nd carrier harmonic component. The flux density in the CI_G is shown in Fig. 12, which demonstrates that the flux reversal takes place at twice the switching frequency.

The simulated circulating currents between the VSCs of the HSCG and the LSCG are shown in Fig. 13(a) and Fig. 13(b), respectively. The integrated inductor offers high inductance to the circulating currents and suppresses them effectively.

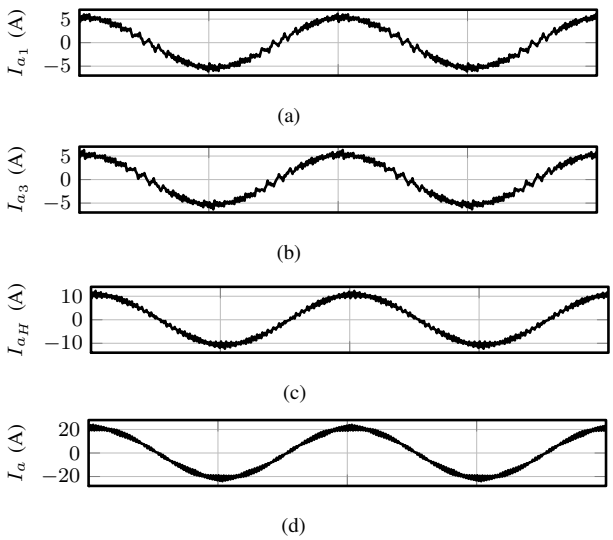

Fig. 14. Simulated current waveforms of phase a at rated operating conditions. (a) Output current VSC_1 (I_{a_1}), (b) Output current VSC_3 (I_{a_3}), (c) Resultant current of the high side converter group (I_{a_H}), (d) Line current I_a.

The additional CI_G is also very effective in suppressing the circulating current between the HSCG and the LSCG, as shown in Fig. 13(c).

The simulated currents of phase a are shown in Fig. 14. The output current of the VSCs of the HSCG are only shown. However, the output current of the VSCs of the LSCG also demonstrates similar current waveform quality. The line current is shown in Fig. 14(d). The peak-to-peak value of the ripple component of the line current is 5.4 A, which is as per the designed value.

B. Experimental Results

The experimental results were obtained for the system specified in Table I. All the VSCs were operated to inject the rated current and they were controlled using the TMS320F28346 floating-point digital signal processor. The output current of both the VSCs of the HSCG (VSC_1 and VSC_3) along with the circulating current ($I_{a_{H,c}}$) are shown in Fig. 15(a). The peak-to-peak value of the $I_{a_{H,c}}$ is 3.8 A, which is slightly higher than the simulated value. This is due to fact that the inherent air gap exists in the cell structure, which reduces the circulating current inductance compared to the simulations. The output current of the HSCG I_{a_H} and the LSCG I_{a_L} are shown in Fig. 15(b). The circulating current between the HSCG and the LSCG is effectively suppressed by the CI_G, as it evident from Fig. 15(b). The integrated inductor also offers the desired line filter inductance to the line current and restricts peak-to-peak value of the ripple component in the line current to the desired value, as shown in Fig. 15(b).

VII. Conclusion

An integrated inductor for parallel interleaved VSCs is proposed in this paper. The proposed inductor suppresses the circulating current between the parallel interleaved VSCs. In

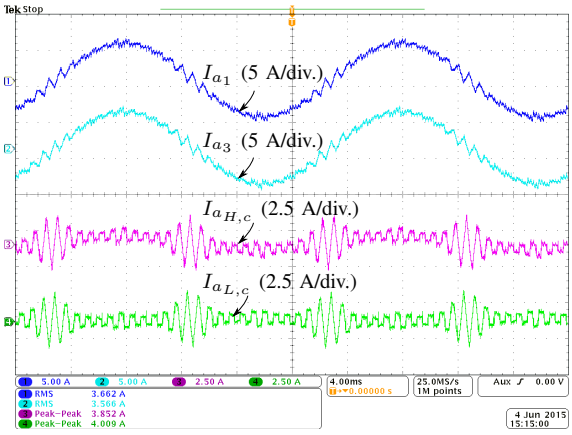

(a)

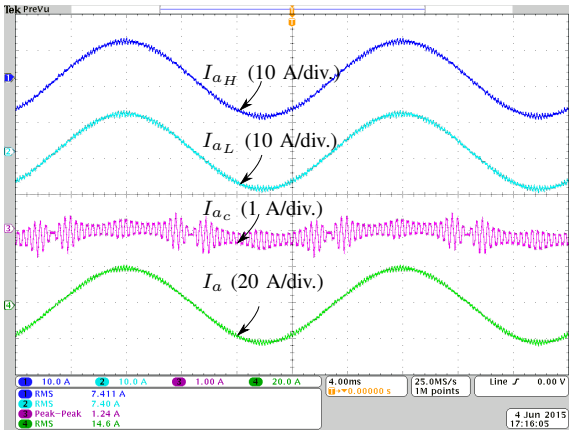

(b)

Fig. 15. Experimental waveforms of the phase a. (a) Ch1: Output current of VSC_1 (I_{a_1}), Ch2: Output current of VSC_3 (I_{a_3}), Ch3: Circulating current between the VSCs of the high side converter group ($I_{a_{H,c}}$), Ch4: Circulating current between the VSCs of the low side converter group ($I_{a_{L,c}}$), (b) Ch1: Output current of the high side converter group (I_{a_H}), Ch2: Output current of the low side converter group (I_{a_L}), Ch3: Circulating current between the high side converter group and the low side converter group (I_{a_c}), Ch4: Line current (I_a).

addition, it offers the desired inductance to the line current as well. The magnetic integration in the case of four parallel interleaved VSCs, connected in a whiffletree configuration is presented. The converters are divided into a high-side converter group and a low-side converter group. The fundamental component of the flux in the cell of the high side converter group is equal to the fundamental component of the flux in the cell of the low-side converter group. Because of the unique arrangement of the coils in the proposed inductor, the fundamental component of the flux of the high-side converter group completes its path through the limbs of the cells of the low-side converter group. Therefore, the need of the dedicated magnetic structure for the return path for the fundamental flux component is avoided. As a result, 22.4% reduction in the volume of the core materials and 12.4% reduction in the volume of the copper can be achieved. The operation of the proposed system has been discussed and the analysis is supported through the simulations and the experimental verification.

REFERENCES

[1] F. Ueda, K. Matsui, M. Asao, and K. Tsuboi, "Parallel-connections of pulsewidth modulated inverters using current sharing reactors," *IEEE Trans. Power Electron.*, vol. 10, no. 6, pp. 673–679, Nov 1995.

[2] S. Miller, T. Beechner, and J. Sun, "A comprehensive study of harmonic cancellation effects in interleaved three-phase VSCs," in *Proc. IEEE Power Electronics Specialists Conference, 2007. PESC 2007.*, 2007, pp. 29–35.

[3] L. Asiminoaei, E. Aeloiza, P. N. Enjeti, and F. Blaabjerg, "Shunt active-power-filter topology based on parallel interleaved inverters," *IEEE Trans. Ind. Electron.*, vol. 55, no. 3, pp. 1175–1189, 2008.

[4] D. Zhang, F. Wang, R. Burgos, L. Rixin, and D. Boroyevich, "Impact of Interleaving on AC Passive Components of Paralleled Three-Phase Voltage-Source Converters," *IEEE Trans. Ind. Appl.*, vol. 46, no. 3, pp. 1042–1054, 2010.

[5] J. Prasad and G. Narayanan, "Minimization of Grid Current Distortion in Parallel-Connected Converters Through Carrier Interleaving," *IEEE Trans. Ind. Electron.*, vol. 61, no. 1, pp. 76–91, Jan 2014.

[6] X. Mao, A. Jain, and R. Ayyanar, "Hybrid interleaved space vector PWM for ripple reduction in modular converters," *IEEE Trans. Power Electron.*, vol. 26, no. 7, pp. 1954–1967, 2011.

[7] K. Xing, F. Lee, D. Borojevic, Z. Ye, and S. Mazumder, "Interleaved PWM with discontinuous space-vector modulation," *IEEE Trans. Power Electron.*, vol. 14, no. 5, pp. 906–917, 1999.

[8] G. Gohil, L.Bede, R.Teodorescu, T. Kerekes, and F. Blaabjerg, "Line filter design of parallel interleaved VSCs for high power wind energy conversion system," *IEEE Trans. Power Electron.*, [Online early access], DOI: 10.1109/TPEL.2015.2394460, 2015.

[9] G. Gohil, L. Bede, R. Teodorescu, T. Kerekes, and F. Blaabjerg, "Design of the trap filter for the high power converters with parallel interleaved VSCs," in *Proc. 40th Annual Conference on IEEE Industrial Electronics Society, IECON 2014*, Oct 2014, pp. 2030–2036.

[10] I. G. Park and S. I. Kim, "Modeling and analysis of multi-interphase transformers for connecting power converters in parallel," in *Proc. 28th Annual IEEE Power Electronics Specialists Conference, 1997. PESC '97 Record.*, vol. 2, 1997, pp. 1164–1170 vol.2.

[11] R. Hausmann and I. Barbi, "Three-phase multilevel bidirectional DC-AC converter using three-phase coupled inductors," in *Proc. IEEE Energy Conversion Congress and Exposition, 2009. ECCE 2009.*, Sept 2009, pp. 2160–2167.

[12] F. Forest, T. Meynard, E. Laboure, V. Costan, E. Sarraute, A. Cuniere, and T. Martire, "Optimization of the supply voltage system in interleaved converters using intercell transformers," *IEEE Trans. Power Electron.*, vol. 22, no. 3, pp. 934–942, 2007.

[13] F. Forest, E. Laboure, T. Meynard, and V. Smet, "Design and comparison of inductors and intercell transformers for filtering of PWM inverter output," *IEEE Trans. Power Electron.*, vol. 24, no. 3, pp. 812–821, 2009.

[14] J. Salmon, J. Ewanchuk, and A. Knight, "PWM inverters using split-wound coupled inductors," *IEEE Trans. Ind. Appl.*, vol. 45, no. 6, pp. 2001–2009, 2009.

[15] B. Cougo, T. Meynard, and G. Gateau, "Parallel Three-Phase Inverters: Optimal PWM Method for Flux Reduction in Intercell Transformers," *IEEE Trans. Power Electron.*, vol. 26, no. 8, pp. 2184–2191, Aug. 2011.

[16] G. Gohil, R. Maheshwari, L. Bede, T. Kerekes, R. Teodorescu, M. Liserre, and F. Blaabjerg, "Modified discontinuous pwm for size reduction of the circulating current filter in parallel interleaved converters," *IEEE Trans. Power Electron.*, vol. 30, no. 7, pp. 3457–3470, July 2015.

[17] G. Gohil, L. Bede, R. Maheshwari, R. Teodorescu, T. Kerekes, and F. Blaabjerg, "Parallel interleaved VSCs: influence of the PWM scheme on the design of the coupled inductor," in *Proc. 40th Annual Conference on IEEE Industrial Electronics Society, IECON 2014*, Oct 2014, pp. 1693–1699.

[18] D. G. Holmes and T. A. Lipo, *Pulse Width Modulation for Power Converters: Principles and Practice*. Hoboken, NJ: Wiley-IEEE Press, 2003.